International Journal of Mass Spectrometry 278 (2008) 59–68

Contents lists available at ScienceDirect

International Journal of Mass Spectrometry

journal homepage: www.elsevier.com/locate/ijms

NanoSIMS μm-scale in situ measurement of $^{13}C/^{12}C$ in early Precambrian organic matter, with permil precision

Ian R. Fletcher[a,*], Matt R. Kilburn[b], Birger Rasmussen[a,1]

[a] School of Earth and Geographical Sciences M006, The University of Western Australia, 35 Stirling Highway, Crawley, WA 6009, Australia
[b] Centre for Microscopy, Characterisation and Analysis M010, The University of Western Australia, 35 Stirling Highway, Crawley, WA 6009, Australia

ARTICLE INFO

Article history:
Received 6 February 2008
Received in revised form 14 August 2008
Accepted 18 August 2008
Available online 26 August 2008

Keywords:
NanoSIMS
$\delta^{13}C$
Precision
Pyrobitumen
Organic matter
C isotopes

ABSTRACT

NanoSIMS is readily able to measure $^{13}C^-/^{12}C^-$ with 1σ internal precision <1‰ and reproducibility ~1‰ on 5 μm × 5 μm areas of solid organic matter, using a rastered Cs^+ primary ion beam and a pair of electron-multiplier secondary ion detectors. Similar results can be obtained on areas as small as 3 μm × 3 μm. Samples smaller than these frame sizes and samples with isotopic complexity on smaller scales can also be analysed, though with poorer precision corresponding to the reductions in analysed surface area. Data reduction requires consideration of the ratio drift resulting from ageing of the $^{12}C^-$ electron multiplier, variations in count rates within the analysed area, and the effects of quasi-simultaneous $^{12}C^-$ arrivals. Samples that do not fill the raster area also require image analysis to determine the effective sample areas; in complex cases the ratios may be better derived from images recorded with long acquisition times.

1. Introduction

The isotopic compositions of carbon and other light elements in many geological samples can now be routinely measured to sub-‰ levels by techniques such as gas-source mass spectrometry of extracted gases [1] or in situ ion microprobe analysis [2–6]. In many cases, this high precision is necessary for resolving geological problems. However, there are also many situations where such precision is not necessary, and where spatial resolution is more critical than data precision [7]. This includes cases where: 1. samples are μm-sized and therefore too small to extract, or to analyse by gas-source mass spectrometry without analyzing multi-grained extracts. These small grains can be analysed in situ by large-radius ion microprobes even though the sample does not entirely fill the primary ion beam 'spot', but there can be accompanying complications that can only be resolved by imaging within the analysis area; or 2. there is μm-scale internal isotopic variability that is greater than the level of analytical precision. The distribution of components within the sample then becomes important, as well as their isotopic composition.

We have assessed the capability of a Cameca NanoSIMS 50 ion microprobe to analyse such samples and demonstrate that it is capable of measuring $\delta^{13}C$ to ~1‰ precision in ancient organic matter, using a Cs^+ primary beam rastered over a 5 μm × 5 μm area and working on a reasonable time scale (<30 min per analysis). Grains smaller than 5 μm can be analysed if their surrounding matrix is C-free, and data can be resolved for components of zoned samples. The practical minimum scale for extracting data of useable precision is probably ~1 μm.

2. Instrument configuration

The instrument configuration was similar to that used by Clode et al. [8], the main difference being that the primary ion source was operated in "normal" mode, i.e., not optimized for small probe diameter (or for increased ion current). Using the 300 μm final aperture (D1-2), the working primary ion currents were 1–2 pA and the nominal spot diameter ~120 nm.

The secondary ion mass analyzer was configured to record $^{12}C^-$, $^{13}C^-$, $^{16}O^-$, and $^{26}[CN]^-$, all with electron-multiplier detectors operating in pulse-counting mode. The first two of these are the principal data species. The $^{16}O^-$ provided a secondary (image) record of matrix/sample distribution and $^{26}[CN]^-$ was used for

* Corresponding author. Present address: Department of Applied Geology, Curtin University of Technology, GPO Box U1987, Perth, WA 6845, Australia.
Tel.: +61 8 9266 9076; fax: +61 8 9266 3153.
E-mail address: I.Fletcher@curtin.edu.au (I.R. Fletcher).
[1] Present address: Department of Applied Geology, Curtin University of Technology, GPO Box U1987, Perth, WA 6845, Australia.

1387-3806/$ – see front matter © 2008 Elsevier B.V. All rights reserved.
doi:10.1016/j.ijms.2008.08.010

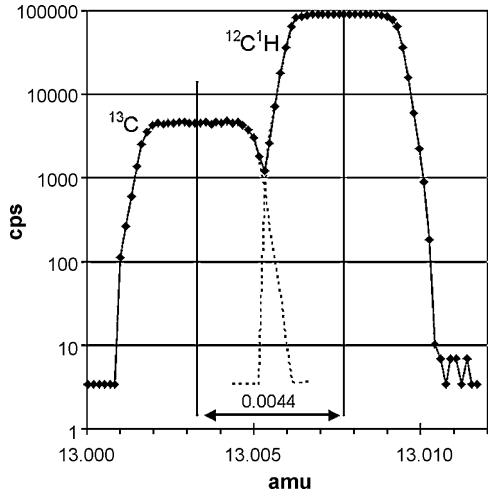

Fig. 1. Mass scan across $^{13}C^-$ and $^{12}C^1H^-$ peaks generated from the K-1 pyrobitumen standard under the operating conditions described in text. The extrapolated flank of each peak is scaled from the corresponding part of the other peak.

real-time imaging, in conjunction with secondary electron imaging, for locating analysis sites. A 40 μm mass analyzer entrance slit (ES-2) was used, beam divergence was limited using an aperture slit of 350 μm (AS-1), and high-side energy filtering cut another 15–20% of secondary beam, resulting in a relative secondary beam transmission of ~45%. Under these conditions, $^{12}C^-$ count rates were $2–3 \times 10^5$ s^{-1} and the mass resolving power was ~8000 (Fig. 1; Cameca MRP = $0.25R{\cdot}\delta M_{10–90}$, where R = radius and $\delta M_{10–90}$ is the mass span of 80% of the peak flank). A 50 μm exit slit was used to record $^{13}C^-$, giving a $M/\delta M$ mass resolution of ~3850 at half-peak height (~2725 at 1% peak height), with the centre of the $^{13}C^-$ peak well isolated from any $^{12}C^1H^-$ tail (Fig. 1). Although a reduced slit width is not necessary for fixing a measurement position on the peak top, it permits the use of the peak centre and simplifies setting the measurement position by a simple half-width offset from the peak flank. There are no potential isobars at masses 12 or 16, and those exit slits were left set at 75 μm.

The pyrobitumen samples were found to be sufficiently conductive that local sample charging was not a problem when operating with this primary beam current. Sample surfaces were coated with 5–10 nm of high-purity Au to provide conductivity across insulating matrix minerals, but it was not necessary to activate the electron gun to neutralize charge at the analysis sites.

3. Samples

3.1. Standard

We have adopted as an in-house carbon isotope standard a vein-filling pyrobitumen ("K-1") from diamond drill-hole KDD1 in the Yerrida Group, in the southeastern Capricon Orogen, Western Australia [9]. K-1 comprises ~3 cm × 2 cm of massive pyrobitumen from a cm-sized quartz-calcite vein (Fig. 2) at the base of a sequence of amygdaloidal basalt, dolerite intrusions and interbedded black carbonaceous shale. Metamorphic monazite in the shale indicates that the succession is ≥1.84 Ga [9]. K-1 is opaque in transmitted light, medium to light grey-brown in reflected light and non-fluorescent. The pyrobitumen is commonly cut by fine fractures filled by calcite and quartz, indicating that it is solid and brittle. Cavity-facing pyrobitumen is cut by arcuate shrinkage cracks and is lined by a thin anisotropic rim. Traces of pyrite and other sulphides are sporadically distributed as minute (1–2 μm) specks throughout the pyrobitumen. Fragments of K-1 analysed by gas chromatography combustion isotope ratio mass spectrometry (GC-C-IRMS) at the University of Waterloo yielded a $\delta^{13}C_{PDB}$ value of $-29.11 \pm 0.24‰$ (95% confidence; $n = 7$).

3.2. Samples

The samples are from diamond drill-hole WRL-1 in the Fortescue Group in the southern Pilbara Craton, northwestern Australia (see [10]). They include bedding-parallel particles of kerogen and irregular masses of pyrobitumen [10]. A detailed description and isotopic characterization of these samples is included in a broader study of kerogen and pyrobitumen from the Fortescue Group, which will be reported elsewhere [11].

3.3. Sample mounts

Samples were mounted as sets of five ~3 mm discs cast into 10 mm epoxy (Korapox®) mounts (Fig. 3a). Each mount included one disc containing standards, which had been drilled from a polished 25 mm standards mount that was fabricated for this purpose. The sample discs were drilled from polished thin sections in which suitable grains had been identified by reflected light microscopy and back-scattered electron imaging.

Mount preparation was modeled on procedures used elsewhere for ion microprobe analyses of samples in polished thin sections [12]. The sample and standard discs were placed face-down on double-sided adhesive tape and a casting cylinder positioned around them. Two types of cylinders were used. Stainless steel cylinders, 5 mm tall with 0.5 mm wall thickness became a component of the mount itself. These guaranteed a clean edge and good electrical conductivity to the mount holder. In contrast, plastic cylinders (10 mm internal) were slipped off after casting. These mounts sometimes require trimming of the face edge, and they rely on electrical conductivity between the Au coat and the facing edge of the mount holder. For both casting methods, placement of the samples is critical, to avoid some of the problems illustrated in Fig. 3b. Even the apparently harmless process of re-positioning

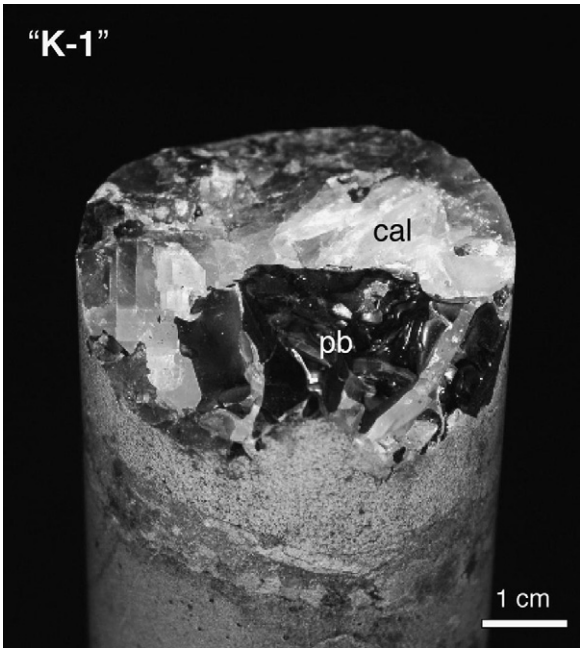

Fig. 2. In-house pyrobitumen $\delta^{13}C$ standard, K-1. The samples analysed by GC-C-IRMS were chipped from different portions of the surface shown. pb = pyrobitumen, cal = calcite.

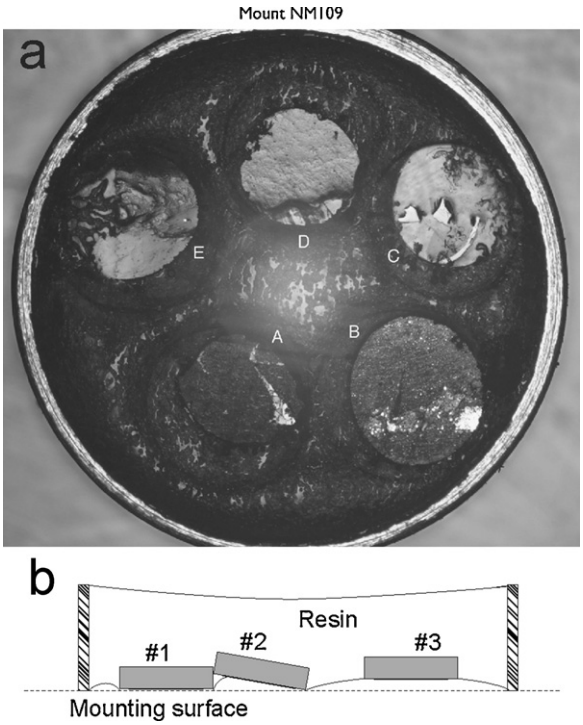

Fig. 3. Steel-ringed sample mount. (a) Reflected-light photograph of a typical 10 mm steel-ringed mount with four sample discs drilled from thin sections and one disc (C) containing the K-1 standard; (b) Edge-view cartoon of potential problems in resin-cast mounts: Sample #1 is well positioned but the adjoining resin surface is not flat; #2 is tilted and therefore also set back, #3 is correctly angled but set back. Problem #2 can be avoided with careful sample layout; #1 and #3 are avoided by using a slip-off plastic mould instead of the steel ring.

a sample on the tape can cause significant misalignment due to distortion of the tape surface when a disc is lifted. With the steel cylinders there was an additional problem that appears to result from contraction of the resin: the resin face, and sometimes also the discs, is drawn up into the steel cylinder. This may relate to curing the resin in an oven, if heat conducted through the steel hastens curing and hence early adhesion to the steel. Faces on the plastic-cast mounts were always flat, and these are preferred.

Prior to analysis, the mounts were cleaned (but not re-polished), imaged in reflected light to enable sample location, Au-coated and outgassed in the NanoSIMS air locks.

4. Data acquisition

4.1. $^{13}C^-/^{12}C^-$ ratios

Each analysis begins by pre-sputtering—rastering the probe across an area larger than the analysis frame in order to remove the Au coat and any residual surface contamination, and to implant Cs into the analysis area to enhance secondary ion emission. The time required for implantation was typically 5–10 min. Before data acquisition the secondary ion beam steering and focusing onto the entrance slit were optimized, and the $^{12}C^-$ and $^{13}C^-$ beams were re-centred using the electrostatic deflectors in front of the exit slits. The magnet was under NMR control and sufficiently stable that peak-centering adjustments between nearby analyses were typically equivalent to <2 μm in collector position (1σ), with no discernible drift during groups of analyses taking 1–2 h. Therefore, peaks were not re-centred during analyses.

Each integration within an analysis consists of the count ratio recorded during a single raster frame (64 × 64 pixels, taking 0.54 s), with corrections for the electronically fixed dead-time of 44 ns based on the total counts of each ionic species recorded within the frame acquisition time. Analyses were compiled in 10–16 blocks of 60–75 integrations, adjusted according to count rates to give >10^6 total $^{13}C^-$ counts and hence <1‰ counting precision in the ratio. The multiple data blocks permitted comparison of (total) counting precision with inter- and intra-block reproducibility. Within-block data rejection was applied on-line, at either 2σ or 3σ level. At both levels the rejection rate was always as expected for a normal distribution, indicating that non-statistical outliers are extremely rare. Data acquisition occupied 10–15 min. All analyses displayed below were on 5 μm × 5 μm areas.

4.2. Images

Ion images were recorded for some of the analysis areas in order to assess the effects of incomplete "coverage" (*p*, defined as the proportion of the analysis area occupied by organic matter) or internal complexity in the samples. Since these images were not intended to be a source of ratio data they were recorded at only modest spatial and counting resolution. All the images referred to in this paper were 128 × 128 pixels, recorded in 2–5 min using either the same primary beam conditions as for ratio data or a smaller final aperture (D1-3; 250 μm) for slightly improved probe focus. These images are sufficient for demonstrating the effects of incomplete coverage, but might be inadequate for recovering data from some complex samples.

5. Uncertainties in sample data

There are many sources of uncertainty in the $\delta^{13}C$ data acquired this way. The absolute minimum uncertainty is defined by counting statistics. Another limit is defined by the block-to-block reproducibility of data within each analysis. Because data rejection has been applied within each block, the reproducibility is commonly better than required by counting statistics. We use the greater of these two values as the precision for each analysis.

The following paragraphs outline systematic and instrumental factors that can affect data. Many of these require modification of the raw $^{13}C^-/^{12}C^-$ data, and each such modification carries some uncertainty that must be propagated to the ratio. However, there is no single procedure for doing this, since some factors are not always relevant. For example, the uncertainty in the absolute $\delta^{13}C$ for the standard is irrelevant if sample data are subjected only to internal comparisons, and the method of propagating the uncertainty in the data for standards depends on whether the sample data are to be used individually or as averages.

Most of the data presented below are shown with 1σ error bars defined by the precision of the individual analyses. Where other uncertainties are involved they are explicitly noted.

6. Instrumental and systematic considerations

6.1. Electron-multiplier ageing

Operating with $^{12}C^-$ count rates of 2–3 × 10^5 s^{-1} causes significant degradation of the electron multiplier in the course of an analytical session, due to ageing of the last dynode. This results in decreasing $^{12}C^-$ response and increasing recorded $^{13}C^-/^{12}C^-$ values (Fig. 4), by as much as ∼5‰ in a ∼10-h session. In some cases, including Fig. 4 and others shown below, there is a suggestion of curvature in the trend but in all these cases the data are statistically consistent with a linear tend (MSWD <1.0 for the linear regression) and higher order regressions were not attempted. Regressions were determined using a least squares fit [13].

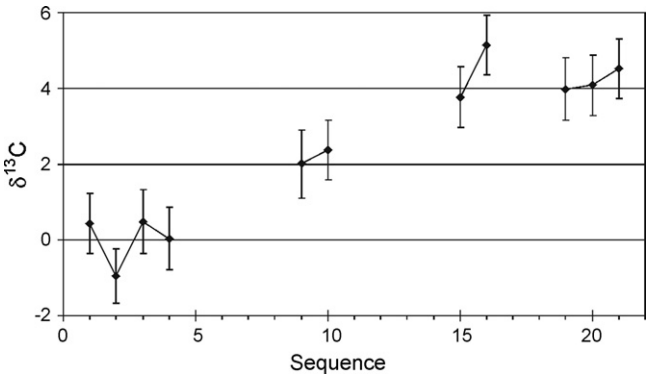

Fig. 4. Drift in $\delta^{13}C$ raw data for K-1 over a ~10 h session with $^{12}C^-$ count rate $\sim 3 \times 10^5\ s^{-1}$. Data are normalized to the average of the first 4 points.

Normalizing the sample data must be done by reference to the standards regression, not a simple average. This is arithmetically simple for the ratio but more complex for the propagated uncertainty since the latter must take into account the uncertainty of the regression slope, resulting in larger uncertainty components in data recorded towards the beginning or end of a session. The time-base for data acquisition is also a consideration. Since it is actually total ion arrivals that determine the degradation rate, and all analyses in a session followed similar setup and analysis sequences, we assume a simple stepped time base, as indicated in Fig. 4. This ignores the difference in count rates for some samples, but any non-linearity introduced by this assumption is insignificant relative to the precision of individual analyses.

The multiplier degradation recorded in Fig. 4 requires an adjustment of ~10 V in the multiplier voltage to restore optimum detector operation. This corresponds to ~1% of the working life of the detector.

6.2. Quasi-simultaneous arrivals

The effects of quasi-simultaneous secondary ion arrivals (QSAs) in electron-multiplier data have been described by [14], who also provide a method for first-order corrections to affected data. Basically, when secondary ionization efficiency is sufficiently high that a single primary ion can generate multiple secondary ions, and secondary ion transmission efficiency is sufficiently high that more than one ion from each "bundle" can reach the detector, the bundle is (incorrectly) registered as a single secondary ion arrival. In the case of $^{13}C^-/^{12}C^-$ measurements, where the effect is dominantly in the $^{12}C^-$ data, the first-order corrected ratio is

$$[^{13}C^-/^{12}C^-]_c = \frac{[^{13}C^-/^{12}C^-]_m}{1 + \{K_m/[1 - K_m/2]\}/2} \quad (1)$$

where $[^{13}C^-/^{12}C^-]_m$ is the measured ratio and K_m is the ratio of secondary $^{12}C^-$ ion current at the collector to primary Cs^+ ion current at the sample surface [14].

The primary beam current reaching the sample (FCo) cannot be measured concurrently with secondary ion data in the NanoSIMS, and it is inconvenient to move the sample stage out of the beam line to monitor the primary beam for each analysis. However, the total secondary ion current entering the primary ion column (FCp) is routinely measured before and after each analysis. For the data reported here, FCo/FCp was recorded before and after each session and on several occasions during the session. This ratio was found to be quite stable under fixed primary column settings, and the average ratio was used with the FCp recorded with each analysis to determine FCo for the analysis.

If the standards and samples are well-matched chemically, errors from QSA effects are minimal, since their secondary ionization efficiencies and $^{12}C^-$ count rates (and hence the critical K_m) will be correspondingly well-matched and data adjustments will be similar, even if large. Unfortunately, this is generally not the case, and some inter-laboratory standards will be essentially unusable with any particular sample when analyses are made by ion microprobes using electron-multiplier detectors. For the mass analyser configuration used here, the QSA correction to $^{13}C^-/^{12}C^-$ for K-1 is ~15‰. Even for other highly mature pyrobitumen and kerogen samples the secondary $^{12}C^-$ output has been observed to differ from K-1 by as much as ~50%, corresponding to a difference of ~6‰ in the QSA correction (though the relationship is not linear). Such differences require that the QSA corrections are accurately determined, and that the uncertainties in the corrections are propagated to the sample $\delta^{13}C$. It is important to note, however, that the uncertainty lies in the difference between samples and the reference standards, not in the absolute magnitude of the corrections. Furthermore, since the QSA corrections are based on count rates, data must be corrected for coverage before either the QSA corrections or their uncertainties are determined.

The $^{12}C^-$ count rates and FCp are so high that the precision of the QSA correction is dominated by the stability of reference measurements of FCo. However, even this is negligible relative to the systematic uncertainty involved in making the QSA corrections. As Slodzian et al. [14] have demonstrated, the theoretical correction is not necessarily accurate, with observed QSA-like data trends ~40% steeper than the theoretical QSA effects for S isotope ratios of sulphide minerals. We have observed no comparable offsets for C in pyrobitumen, for which ionization efficiency and hence QSA effects are less than half those for S in the samples analysed by Slodzian et al. [14], but cannot claim that they are absent. If the model used for QSA corrections in C is inaccurate by, say, 25%, the final data for samples with $^{12}C^-$ count rates ~35% lower than the standard would be inaccurate by ~1‰. This is a systematic (absolute, as opposed to statistical) uncertainty.

6.3. Incomplete coverage

Valid data can be acquired from samples that do not fill the analysis raster area, provided that the sample matrix does not generate a significant number of C^- secondary ions. When coverage is incomplete ($p < 1$), there is a loss of precision corresponding to the reduction in total secondary ion counts but this can be redressed, if necessary, by using longer integration times. It is essential to calculate dead-time corrections on the basis of actual count rates, not frame averages. The C^- beams are not continuous if coverage is incomplete, since no C^- is generated when the rastered primary beam does not strike the sample. The C^- count rates are higher than the recorded frame averages, and the frame integration time t used for on-line dead-time corrections should be replaced by pt. The primary frame-by-frame data cannot be retrieved so the corrections must be made to the uncorrected block-by-block or compiled data, or by making a first-order adjustment to the dead-time corrected output data. There is no significant difference in the results from the two methods of calculation and the latter has been used, to minimize the need for data transfer.

Less obviously, but equally important, the QSA correction must also be modified to take account of incomplete coverage. The K_m term in Eq. (1) is the ratio of $^{12}C^-$ current at the collector to Cs^+ current at the sample surface. Both currents are presented in data outputs as though they are continuous, which is not true for the C^- beams if coverage is incomplete. In order to apply an appropriate QSA correction, the recorded C^- count rates must be scaled up according to the coverage, i.e., K_m must be replaced by $K_t = [K_m/p]$.

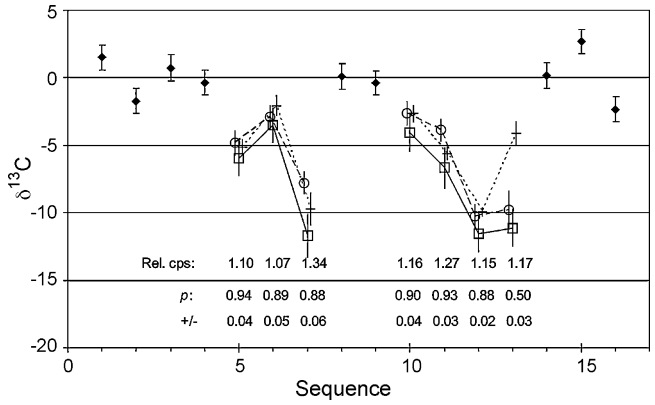

Fig. 5. Effects of QSA and incomplete coverage. All data are corrected for electron-multiplier dead-time and ageing, and are normalized to ♦. Sample data are shown (with points offset for clarity) as: ◯ = before QSA correction, with internal 1σ precision; □ = QSA-corrected, with the systematic error that would propagate from a 10% error in the QSA model; + = incorrect results, due to not adjusting the QSA correction to account for p, shown with the uncertainty component that would propagate to □ from the uncertainty in p. "Rel.cps" is the true count rate from the samples, relative to the average count rate for the standards in this session.

Fig. 5 illustrates some effects of QSA and coverage adjustments to QSA corrections. The data are from a multi-component sample, so they are more scattered than the standards, even though the standards in this session were less reproducible than usual. The starting data (◯) have been corrected for dead-time and normalised to the standards trend, and are shown with 1σ measurement precision. The secondary ionization efficiency for the samples varies up to 35% from that of the standard, so when QSA corrections are applied there are some significant offsets in the data (□). The error bars on the corrected data show only the error that would propagate from a 10% error in the QSA model. If a simple QSA correction had been applied without adjustment for coverage, which ranges down to ~50%, the results (+) would be significantly inaccurate in some cases. These (incorrect) points have been used to display the uncertainties that would propagate through the QSA correction (to □) from the listed uncertainties in p.

An alternative way to deal with incomplete coverage is to acquire data in an image format then use the pixel data within selected areas in the images. This allows a more conservative selection of the analysed portion of sample surface, making it easy to avoid sample edges or areas of complexity, but with a corresponding loss of overall counting precision. A computation equivalent to a coverage correction is still required, and NanoSIMS software deals with this by the simple expedient of counting the pixels and hence determining the integration time corresponding to the total ion counts within the selected image area.

The coverage problem is not restricted to measurements using rastered primary beams. For a stationary primary beam the secondary beam is indeed continuous, and the recorded secondary beam current is a true running average. However, if the probe spot is not filled by sample, only a portion of the primary beam is being used to generate secondary ions. If the secondary ions are counted using electron multipliers, the required correction to K_m is again proportional to coverage, i.e., the same K_t is required as for rastered-beam measurements.

6.4. Determining coverage from images

6.4.1. Simple geometry

The only reliable way to determine p is by imaging the analysis areas. In cases such as shown in Fig. 6a, where the sample geometry is simple, pencil-and-ruler measurements would be adequate. More generally, if the signal intensity from the sample is reasonably uniform a simple digital solution can be derived from the count rates for each pixel. Fig. 6b shows the $^{12}C^-$ pixel-count against the range of observed counts/pixel in Fig. 6a. There are three dominant components to the curve: a high-count peak from pixels completely within the sample, a zero-count half-peak from pixels remote from the sample, and tails on both these curves from pixels overlapping the sample edge. The high-count side of the high-count peak fits the shape of a Gaussian curve (modeled in Fig. 6b), but the peak is about twice as wide as the Gaussian curve determined from the peak count rate. The additional dispersion might arise from minor compositional variations in the sample.

Pixels recording half the peak count rate are interpreted to be centred on the sample edge, and a simple count of pixels above and below this count rate defines p. Even though the peak count rate is not defined to high precision, the uncertainty in p is small. In this case, an error in the peak count rate corresponding to the half-width (at half-peak height) of the modeled curve propagates to an error of 0.02 in $p = 0.78$ and <0.1‰ in $\delta^{13}C$.

6.4.2. Complex geometry

The method just described is less reliable for finely dispersed samples, partly because a larger proportion of pixels include sample boundaries. Fig. 7 shows a case where pyrobitumen is finely interspersed with silica matrix. The distribution of $^{12}C^-$ count rates (Fig. 7c, derived from Fig. 7a) is not clearly partitioned as in Fig. 6b, and there appears to be some fine structure. The calculated p is correspondingly less precise, regardless of how it is determined. Applying the same partitioning criteria as for Fig. 6 gives $p = 0.79 \pm 0.06$.

In principle, the $^{16}O^-$ image (Fig. 7b) is complementary to the $^{12}C^-$ image and could provide a second determination of p. However, interpreting the matrix image is more complex, and in this case applying the same partitioning criteria as for $^{12}C^-$ gives $p \sim 0.35$, distinctly different from the value derived from $^{12}C^-$. Two sources of complication are apparent: the matrix is unlikely to be monomineralic, with different components giving different $^{16}O^-$

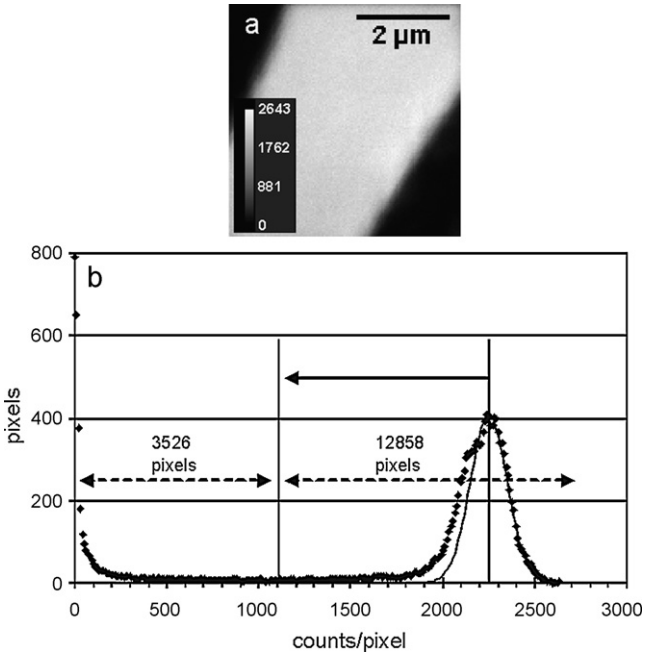

Fig. 6. Determining coverage (p) from a sample with simple geometry and composition. (a) $^{12}C^-$ ion image of the analysed area; (b) schematic illustration of the method of calculation.

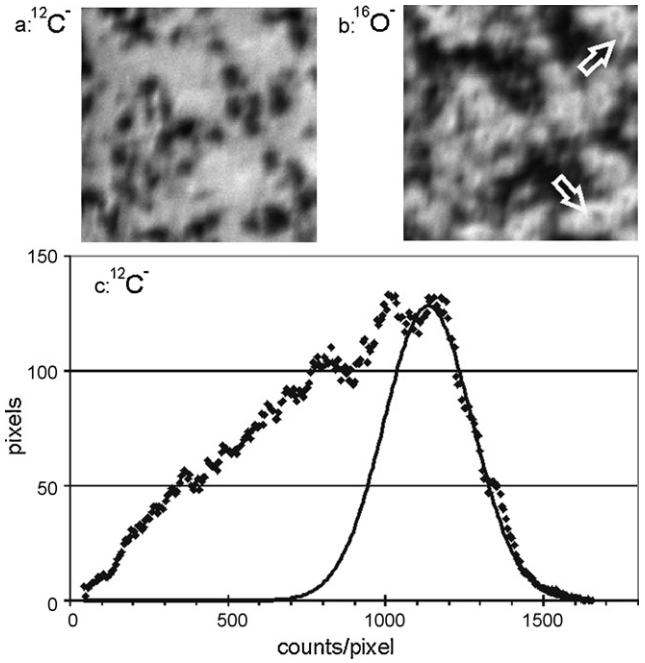

Fig. 7. Ion images and $^{12}C^-$ count distribution for a sample with complex geometry. (a) $^{12}C^-$ ion image; (b) $^{16}O^-$ ion image, with arrows indicating two of the dark spots within O-bright areas, possibly due to surface charging; (c) count distribution from (a), used to determine p. Images 5 μm × 5 μm. Grey scales in (a) and (b) are linear.

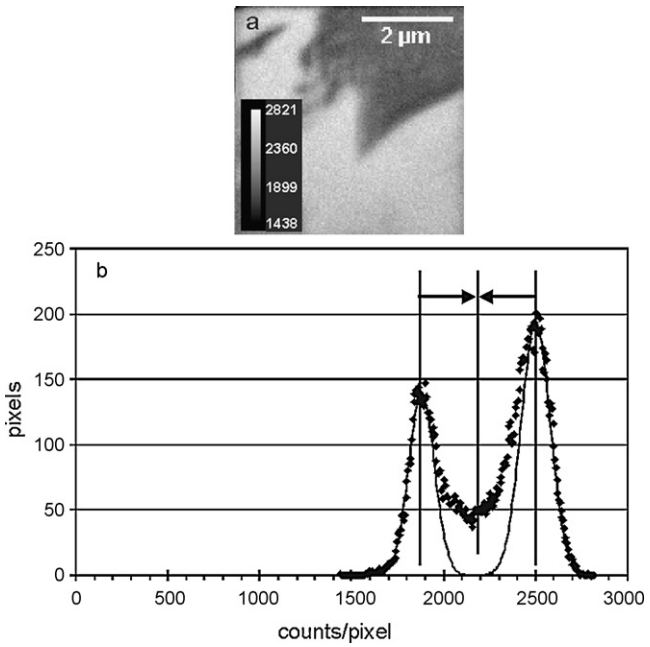

Fig. 8. Determining relative areas in a 2-component sample. (a) $^{12}C^-$ ion image; (b) schematic of the method for determining proportions.

signal intensities, and ion emission seems to be suppressed in larger areas of matrix (e.g., dark spots indicated in Fig. 7b) due to local charging. Imaging non-conductive matrix cannot compensate for limitations in the determination of p from images of conductive samples.

6.4.3. Multi-component pyrobitumen

Similar procedures can be applied when a sample contains a small number of components that give differing C^- signal intensities. The pyrobitumen imaged in Fig. 8a has two main compositional components separated by an irregular boundary, but no exposed matrix. At the boundary there are patches with intermediate $^{12}C^-$ signal intensity, which might be an additional component but which we assume, for simplicity, are mixtures of the two main components.

Determining the areas of the two components is illustrated in Fig. 8b. There are two peaks in the $^{12}C^-$ intensity distribution, with tailing between them and some complexity due to the fine mixing at the boundary. The modeled curves define the average $^{12}C^-$ intensity for the two components, and the midpoint between these is interpreted as data from pixels that straddle the boundary. The plotted curves give a 60:40 split between areas of the components. There is some uncertainty due to the complexities between the main peaks, but the proportions are not highly sensitive to this. A one half-width error in defining the centre of either of the peaks translates to an error of ~2% in the calculated proportions.

Mixture modeling gives

$$\delta^{13}C_m = \frac{\delta^{13}C_d[p_{rel}E_{rel}] + \delta^{13}C_b}{p_{rel}E_{rel} + 1} \quad (2)$$

for the measured composition $\delta^{13}C_m$, where $\delta^{13}C_{d,b}$ are the compositions of the two components (C^--dark and C^--bright, respectively), p_{rel} is the ratio of the two areas (40/60 = 0.67 in this case) and E_{rel} is the ratio of the ionization efficiencies (1880/2500 = 0.75). The sample compositions cannot be determined from a single mixed analysis, but there are the only two

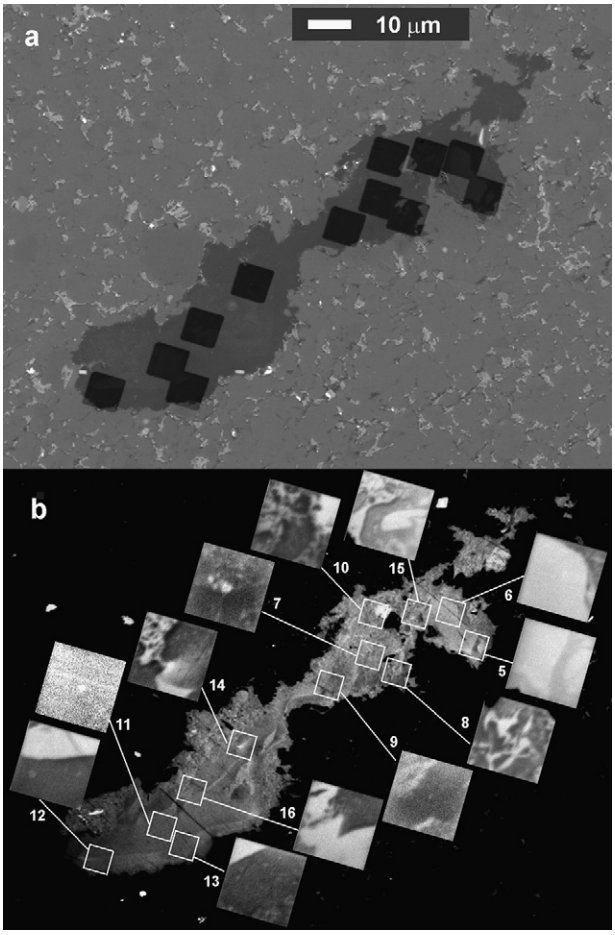

Fig. 9. (a) Post-analysis back-scattered electron image of a complex pyrobitumen grain, showing the outlines of NanoSIMS pre-sputter areas; (b) high-contrast reflected light image of the same grain, with (inset) $^{12}C^-$ images of areas analysed by NanoSIMS. Analysis numbers in (b) correspond with Fig. 10.

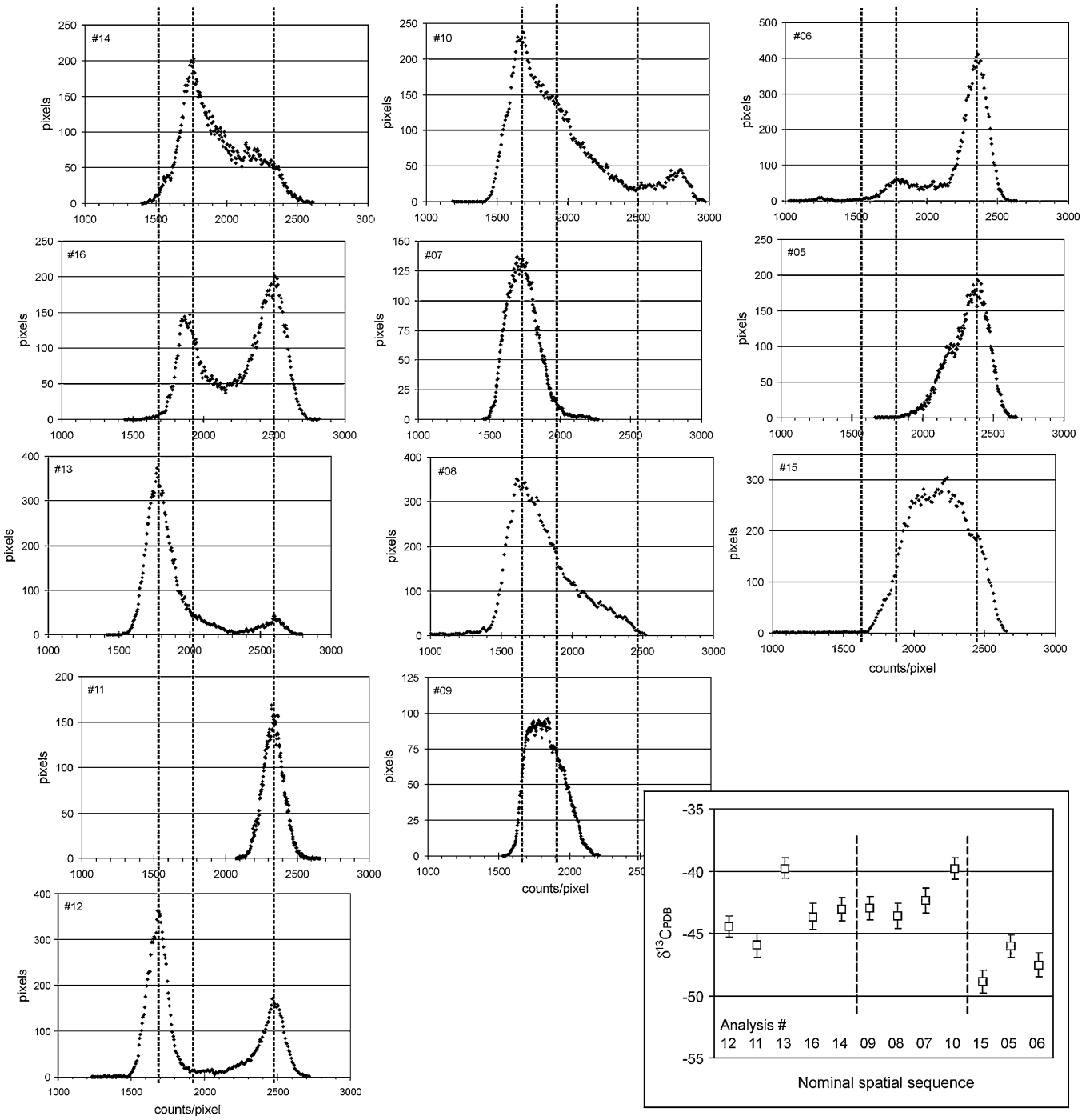

Fig. 10. Count rate distributions from the $^{12}C^-$ images in Fig. 9b, grouped according to location in the grain. Data for #05, #08 and #15 have been truncated, deleting low-count data from mineral inclusions. The vertical lines mark three sample components apparent in images and the left hand column of this figure. A fourth component is required by #10. The complex distributions for #05, #09 and #15 can be modeled with contributions from additional components. A possible correspondence between the three columns, shown by the vertical lines, is based largely on count rates. The alignment of frames #09 and #15, in particular, is speculative. Inset: $\delta^{13}C_{PDB}$ data from the imaged areas, grouped as in the three columns of this figure. Analysis numbers correspond with Fig. 9b.

unknown terms in (2), so in principle they can be extracted from two measurements (with different p_{rel}) or they can be determined by modeling the mixing curve for a suite of data.

6.4.4. Highly complex samples

Fig. 8a is one analysis in a suite of 12 from a ~120 μm single grain (Fig. 9) that displays a range of geometric interrelationships between numerous distinct components, ranging from sharp linear boundaries to some that are highly irregular and some that appear to be diffuse. The complexity was first identified in the isotopic analyses and later characterized in more complete spatial detail by high-contrast optical reflectance imaging (Fig. 9b). The $\delta^{13}C_{PDB}$ values from the NanoSIMS analyses vary from −40‰ to −49‰, and the count rate distributions (Fig. 10) suggest a minimum of four, and possibly more than five, discrete components.

There is a degree of correspondence, but no definitive correlation, between compositional components identified by count rates in Fig. 10 and the $\delta^{13}C$ data (Fig. 10 inset). Analysis #11 lies within

a single zone, and it would be possible to deconvolve the data from some of the simpler mixed areas, but the multi-component analyses (e.g., #10, #15) cannot be resolved numerically from a practical number of analyses. Even where the mixing is superficially simple there are complications. In particular, isotopic data for #11, #12 and #13 do not conform to a two-component mixing line, and the marginal zone in #13 is probably not continuous with that in #12. In reflected light the boundary is less distinct at #13, and the marginal zone is darker.

For samples as complex as this, $\delta^{13}C$ data can probably be best obtained by sampling from long-duration or "stacked" isotope images.

6.4.5. Finely divided inclusions

There might be additional issues involving coverage when the sample and matrix are finely divided.

Consider, as a starting point, an area of simple sample such as in Fig. 6a. If the areas of matrix were fragmented and distributed through the sample (or, conversely, the sample was fragmented and scattered around the same analysis frame) leaving p unchanged, the required modification to the QSA correction also remains unchanged. This condition persists to progressively finer division of the matrix and sample, provided p remains constant.

On the other hand, if the two mineral components were mixed at the molecular level, i.e., if the same elemental components were co-precipitated as a third mineral, the sample would be uniform and no coverage correction would be required.

There must be some crossover point between these states, which is possibly a simple question of physical dimension rather than of chemical composition or crystallographic structure. As the diminishingly small inclusions reach the size of the zones sputtered/activated by single primary ion impacts (<~10 nm), there is a transition from discrete-area to integrated-sample response. This is below the spatial resolution of any practical ion imaging (~50 nm), so there could be cases where samples appear to be uniform but coverage corrections should be applied. Identifying such cases would be very difficult.

6.5. Pre-sputtering issues

The degree of pre-sputtering employed has an effect on absolute ionization efficiencies, but no direct effect on the relative ionization efficiencies of $^{12}C^-$ and $^{13}C^-$. However, the pre-sputter conditions can affect the recorded ratios indirectly. Problems arise if pre-sputtering is inadequate, resulting in rapidly rising C^- beams while the secondary ion focusing and steering are being optimised. Similarly, a decreasing beam can occur following pre-sputtering using a boosted primary beam. The problems are thought to arise from the "top, left, right" peak-centering procedures applied to the secondary beam focus and steering, and possibly also to peak centering at the collector. If the secondary beam intensity is changing, the peak half-heights are changing and these points cannot be located correctly; instead, the software chooses a position where the (changing) peak flank is half the height of the starting peak intensity. There is a corresponding offset in the selected central value.

This is not a significant problem when analyses are operator-controlled, because the drift in beam intensity is readily observed and the centering process can be delayed. Problems are more likely when analyses are under computer control. Fig. 116 shows the data for standards recorded in one overnight session when inadequate pre-sputtering was applied. The data used as reference measurements are isolated single analyses, whereas the "sample" data are from second analyses on some of the same sites, re-visited after various delays. The secondary beam intensities were rising quickly

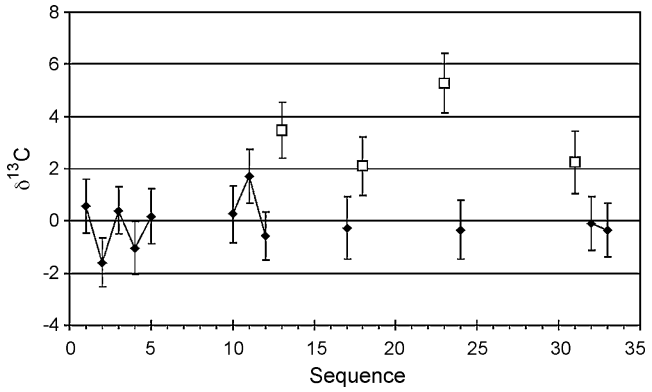

Fig. 11. Differences between analyses with consistent but inadequate pre-sputtering (♦), and later analyses in some of the same areas (□). All data are from K-1 and are normalised to the linear trend through ♦.

during tuning for the reference analyses, but not for the repeats. The reference analyses were all similarly affected, and their data conform to a single $^{13}C^-/^{12}C^-$ ageing trend (MSWD = 0.8). Data from the repeat analyses are clearly different from the reference trend, which we attribute to the difference in secondary beam optimization. Some of the scatter amongst the repeat analyses might be attributable to small differences in analysis locations for the re-visited sites.

6.6. Closely spaced analyses

With any ion probe analyses there are potential problems when analyses are closely spaced, because each analysis can change the local surface conductivity. This is not a problem for pyrobitumen

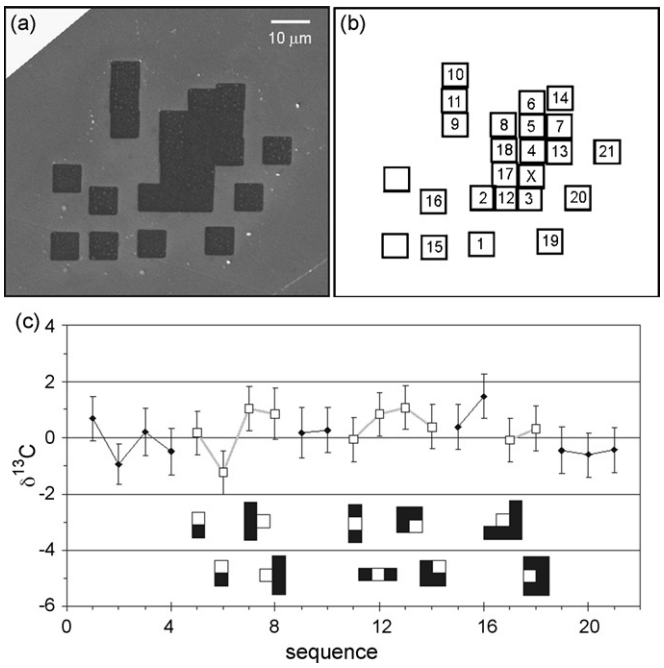

Fig. 12. Close-spaced analyses of the K-1 standard, with data acquisition from 5 μm × 5 μm areas within 7.5 μm × 7.5 μm pre-sputtered patches. (a) Post-analysis SEM image of the analysis area; (b) Analysis sequence. 'X' is a patch that was pre-sputtered to prepare for analysis 17, without recording data. The unlabeled patches were not part of this experiment; (c) Data sequence. ♦ = data from isolated analysis sites, used as reference standards; □ = data from sites that lie against previous sites, as shown in (b) and in the diagram below each datum. All data normalized to the linear ageing trend for ♦, and shown with 1σ internal precision.

under the conditions used in this study, presumably because the samples are sufficiently conductive that there is no reliance on having close edges with the Au coat. Therefore, it is possible to use closely spaced (even overlapping) analyses if this is desired for complex, small samples. To confirm this immunity from edge effects, a series of analyses was made in sites that had various edge relationships with previous analyses (Fig. 12a and b). The data (Fig. 12c) are clearly not affected by close proximity to Au-free areas.

6.7. Minimum analysis area

Samples such as those shown in Figs. 7–9 make it clear that using smaller analysis areas, even to <1 μm × 1 μm, would be advantageous in some cases. However, it is generally acknowledged that at the small-area limit (namely using a stationary primary ion beam spot), NanoSIMS isotope ratio data for light elements have unacceptably poor reproducibility (cf. Pb; [15]). To test this limit for rastered-area analyses we have included analyses of K-1 on both 3 μm × 3 μm and 1 μm × 1 μm areas in two analytical sessions. The data recorded at 1 μm × 1 μm are clearly unreliable, with up to ~10‰ variations between sequential analyses on single sites, and similar differences between sites. Data for 3 μm × 3 μm spots are equivocal. One short session (three analyses on each of two sites) gave data offset ~5‰ from 5 μm × 5 μm K-1 data, but with satisfactory reproducibility (1σ = 1.1‰; MSWD = 1.4). A longer session (n = 14) gave much poorer reproducibility (1σ = 3.1‰), but in this case there were complications from a combination of a pitted mount surface and insufficient Au coat. More work is needed to ascertain the minimum working area for rastered-beam isotopic analyses, but it is probably ~3 μm × 3 μm.

7. Summary

These experiments were carried out using pyrobitumen samples, typical of non-volatile oil residues. The procedures are not universally applicable because of the matrix dependence of C^- secondary ion yields. In particular, the C^- ionization efficiency in carbonate minerals is orders of magnitude lower than for organic matter and it would be impractical to obtain ‰-precision data from inorganic carbonates using the primary ion beam conditions of this study. However, most of the following points would apply to any organic samples.

Using a basic configuration for the primary ion column, secondary ion count rates are such that the benchmark of measuring $^{13}C^-/^{12}C^-$ to 1‰ (1σ) precision is readily achieved. The secondary ion focusing and transfer configuration required to achieve robust resolution of $^{13}C^-$ from $^{12}C^1H^-$ is also fairly routine, requiring only a modest reduction (~50%) in secondary ion transmission.

After corrections are made for data drift during each analytical session, the reproducibility of $^{13}C^-/^{12}C^-$ measurements is also ~1‰. Therefore, collecting more data within any single analysis, to provide internal precision appreciably better than 1‰, is not justified unless there are multiple components within the analysed areas of sample. The drift derives predominantly from ageing of the electron multiplier used to record $^{12}C^-$, and can be as much as ~0.5‰ h^{-1} under the conditions used for this study. The drift is automatically monitored by the interspersed measurements of $\delta^{13}C$ reference standards. Uncertainties in determining the regression slope should be propagated to the sample data in conjunction with the uncertainty in the mean of the reference data. Consequently, the total uncertainty in individual analyses made near the beginning or the end of a session can be somewhat larger than for data recorded mid-session.

Both the secondary ionization efficiency for C^- and secondary ion transmission are high enough that the measured ratios require adjustment for the counts missed because of quasi-simultaneous $^{12}C^-$ impacts on the electron multiplier. For carbon, the first-order QSA correction of [14] appears to work adequately, with adjustments up to ~15‰ under our operating conditions. This contrasts with the case for sulphur in sulphide minerals, which requires corrections several times greater because of its higher secondary ionization efficiency, and for which the first-order correction is inadequate [14].

The minimum practical analysis area appears to be ~3 μm × 3 μm. Samples smaller than this, elongate samples too thin to fill a square frame, or samples finely mixed with non-carbonaceous matrix, can be analysed but with a loss of precision corresponding to the decrease in the area of sample analysed. Such analyses require accurate determination of the actual sample area, since this determines the secondary ion count rates and hence the corrections for dead-time and QSA. The area can be determined from ion images recorded immediately after (or perhaps before) the ratio analysis.

Ion imaging can also delineate areas of differing sample chemistry, which may also have different $\delta^{13}C$, by making use of their different $^{12}C^-$ ionization efficiencies. If such cases involve only two (or perhaps three) compositional zones, the corresponding $\delta^{13}C$ can be determined arithmetically or graphically from a suite of mixed analyses. For more complex samples, the only practical method of obtaining $\delta^{13}C$ for the various components is to extract the ratios from zones within long-period ion images. In practice, this requires "stacked" images.

One feature of the samples analysed here that is probably uncommon amongst organic samples is their electrical conductivity. These high-temperature residues are sufficiently conductive that surface charging is not an issue, and analyses can be performed on areas that are immediately adjacent or overlapping.

These results show that NanoSIMS is capable of measuring $\delta^{13}C$ to ~1‰ precision and reproducibility in pyrobitumen as small as ~5 μm, using a rastered Cs^+ primary ion beam and a pair of electron-multiplier secondary ion collectors in static collection mode. The minimum sample size for analyses of this quality is probably about 3 μm, but potentially useful data can be obtained from samples down to ~1 μm, with decreased precision corresponding to the reduced total $^{13}C^-$ ion counts, by analyzing over a larger area. Finely divided samples and complex mixed samples can also be analysed by making use of the imaging capability of NanoSIMS.

The in-house $\delta^{13}C$ standard K-1 appears to be homogeneous. It will be tested further, and additional reference data acquired, with a view to making small splits available for interlaboratory calibrations. Its use may be limited to ion probe and laser ablation analyses, during which it is relatively simple to avoid any traces of cross-cutting calcite.

Acknowledgements

We are indebted to F. Hillion for extensive advice on NanoSIMS analytical procedures for isotope ratio measurement. He and two anonymous reviewers provided comments on an earlier version of this paper. The K-1 standard is from Rio Tinto (then CRA) KDD-1 drillcore, provided by G. Broadbent. NanoSIMS instrument time was partly funded by TAP funds from the Australian NANO-NMRF. The authors acknowledge the facilities, scientific and technical assistance of the Australian Microscopy & Microanalysis Research Facility at the Centre for Microscopy, Characterisation & Analysis, The University of Western Australia, a facility funded by The University, State and Commonwealth Governments.

References

[1] M.A. van Zuilen, A. Lepland, G. Arrhenius, Nature 418 (2002) 627.
[2] L.R. Riciputi, B.A. Paterson, R.L. Ripperdan, Int. J. Mass Spectrom. 178 (1998) 81.
[3] J. Farquhar, E. Hauri, J. Wang, Earth Planet. Sci. Lett. 171 (1999) 607.
[4] C.H. House, J.W. Schopf, K.D. McKeegan, C.D. Coath, T.M. Harrison, K.O. Stetter, Geology 28 (2000) 707.
[5] E.H. Hauri, J. Wang, D.G. Pearson, G.P. Bulanova, Chem. Geol. 185 (2002) 149.
[6] B.S. Kamber, M.J. Whitehouse, Geobiology 5 (2007) 5.
[7] S.J. Mojzsis, G. Arrhenius, K.D. McKeegan, T.M. Harrison, A.P. Nutman, C.R.L. Friend, Nature 384 (1996) 55.
[8] P.L. Clode, R.A. Stern, A.T. Marshall, Microsc. Res. Tech. 70 (2007) 220.
[9] B. Rasmussen, I.R. Fletcher, Earth Planet. Sci. Lett. 197 (2002) 287.
[10] B. Rasmussen, Geology 33 (2005) 497.
[11] B. Rasmussen, I.R. Fletcher, J.J. Brocks, M.R. Kilburn, Nature (in press).
[12] N. Rayner, R.A. Stern, Curr. Res. 2002–F10 (2002) 1.
[13] D. York, Earth Planet. Sci. Lett. 5 (1969) 320.
[14] G. Slodzian, F. Hillion, F.J. Stadermann, E. Zinner, Appl. Surf. Sci. 231–232 (2004) 874.
[15] R.A. Stern, I.R. Fletcher, B. Rasmussen, N.J. McNaughton, B.J. Griffin, Int. J. Mass Spectrom. 244 (2005) 125.